REVISION 2

(Ca-Y)-phosphate inclusions in apatite crystals from Archean rocks from the Barberton Greenstone Belt and Pilbara Craton: first report of natural occurrence

ŁUKASZ BIRSKI[1], RICHARD WIRTH [2], EWA SŁABY[1], ALICJA GIERA[1], AIVO LEPLAND[3,4,5], AXEL HOFMANN[6] AND ANJA SCHREIBER[2]

[1]Institute of Geological Sciences, Polish Academy of Sciences, Research Center in Warsaw, Twarda 51/55 00-818 Warsaw, Poland
[2]GeoForschungsZentrum Potsdam, Telegrafenberg, 14473 Potsdam, Germany
[3]Geological Survey of Norway, Sluppen, 7491 Trondheim, Norway
[4]Institute of Geology, Tallinn University of Technology, Ehitajate tee 5, 19086 Tallinn, Estonia
[5]Center for Arctic Gas Hydrate, Environment and Climate, Langnes, 9037 Tromsø, Norway
[6]Department of Geology, University of Johannesburg, Auckland Park, 2006 Johannesburg, South Africa

ABSTRACT

Here, we report the first occurrence of two (Ca-Y)-phosphate phases in apatite crystals from ancient rocks from both the Barberton greenstone belt and the Pilbara Craton. First, a cubic $Ca_3Y(PO_4)_3$ phase was observed in a sample of silicified tuff from the Mendon Formation from the Barberton greenstone belt. A second phase, corresponding to a synthetic compound with the formula $CaYP_7O_{20}$, was observed in a sample of black banded chert from the Hooggenoeg Formation of the Onverwacht Group and in a sample of chert from the Strelley Pool Chert Formation (East Pilbara Terrane). Based on the presence of these phosphates and specific textures revealed by transmission electron microscopy, we argue for the importance of dissolution-reprecipitation processes in the formation of these phosphate phases. Temperature was likely not the primary parameter controlling the crystallization of the $Ca_3Y(PO_4)_3$ and $CaYP_7O_{20}$ phases. Instead, the REE-F complexes in an H_2O solution and the specific budget of REEs and Y in apatite were likely responsible for the nucleation and formation of the (Ca-Y)-phosphate phases in the Archean rocks of the Barberton greenstone belt and Pilbara Craton.

KEYWORDS: Barberton, apatite, TEM, (Ca-Y)-phosphate

INTRODUCTION

More than 200 species of phosphate minerals are known to exist in nature, and these minerals include apatite (e.g., Hughes and Rakovan 2002), monazite (e.g., Ni et al. 1995) and xenotime (e.g., Ni et al. 1995). Here, we report the first occurrence of two (Ca-Y)-phosphate phases in apatite crystals from the ancient rocks of both the Barberton Greenstone Belt and the Pilbara Craton. First, a cubic $Ca_3Y(PO4)_3$ phase was observed in a sample of silicified tuff from the Mendon Formation dated at 3.298 Ga (Knauth and Lowe 2003). This high-temperature phase was first described as a synthetic material by Fukuda et al. (2006). $Ca_3Y(PO4)_3$ is isostructural with eulytite ($Bi_4(SiO_4)_3$) and is cubic (space group $I\bar{4}3d$) with a = 0.983320(5) nm, V = 0.950790(8) nm^3, Z = 4 and D_x = 3.45 Mg m^{-3}. Data on the synthesis and the stability of synthetic $Ca_3Y(PO_4)_3$ suggest that the crystallization of this phase begins at temperatures above 1215 °C at atmospheric pressure (Fukuda et al. 2006; Matraszek and Radomińska 2014). The second phase examined in this study has an empirical formula of $(Ca_{0.726}Y_{0.274})(Ca_{0.274}Y_{0.726})P_7O_{20}$, ideally $CaYP_7O_{20}$, and was observed in a sample of black banded chert from the Hooggenoeg Formation of the Onverwacht Group dated at 3.445 Ga (Knauth and Lowe 2003) and in a sample of chert from the Strelley Pool Chert Formation (East Pilbara Terrane) dated at 3.43 Ga (van Kranendonk et al. 2008). This ultraphosphate is a member of a group of chemical compounds that are characterized by ultraphosphate anions with the general formula $[P_{(n+2)}O_{(3n+5)}]^{n-}$. Anions are known for n = 2, 3, 4, 5 and 6, yet only as experimental run products. According to our knowledge, no ultraphosphate was reported in natural samples. The properties of ultraphosphate are best known for minerals with the general formula $(P_5O_{14})^{3-}$, e.g. YP_5O_{14}, NdP_5O_{14} and LuP_5O_{14} (e.g., Mbarek et al. 2009). Calcium and yttrium ultraphosphate crystallizes in the monoclinic system (space group C2/c), with the following cell parameters: a = 24.666 Å, b = 6.850 Å, c = 10.698 Å, and β = 107.40° (Hamady and Jouini 1994). The phase was obtained artificially by reacting a mixture of $CaCO_3$, Y_2O_3 and $NH_4H_2PO_4$ (with Ca:Y:P proportions of 1:2:17) at 450 °C for twelve hours (Hamady and Jouini 1994). Both phases, $Ca_3Y(PO_4)_3$ and $CaYP_7O_{20}$, were identified and characterized using transmission electron microscopy (TEM).

GEOLOGICAL SETTING

The Barberton greenstone belt (BGB) is located in the Kaapvaal Craton of South Africa. It comprises one of the best preserved and oldest supracrustal successions (3.55–3.22 Ga) (Kröner et al. 1991). The BGB is subdivided into three stratigraphic units (the Onverwacht, Fig Tree and Moodies groups) and consists of a sequence of mafic to ultramafic lavas and metasedimentary rocks metamorphosed under greenschist-facies conditions (Tice et al. 2004). Locally, close to the contact with the surrounding granitoid domes that intruded the supracrustal rocks of the BGB during several episodes of magmatism at 3.45, 3.22, and 3.10 Ga (Furnes et al. 2011), the pressure-temperature (P-T) conditions reached those of amphibolite facies (Kamo and Davis 1994).

The East Pilbara Terrane of the Pilbara Craton is located in Western Australia. This region contains a variably metamorphosed mafic and ultramafic greenstone succession and intrusive granitic dome structures. The supracrustal rocks have been subdivided into the Warrawoona (3.52–3.43 Ga), Kelly (3.43–3.31 Ga), Sulphur Springs (3.27–3.24 Ga) and Soanesville groups (ca. 3.20–3.17 Ga) (van Kranendonk et al. 2008). The regionally extensive sedimentary Strelley Pool Formation, composed primarily of sandstone, is defined as the basal unit of the Kelly Group (Hickman 2008; Wacey et al. 2010)

SAMPLE DESCRIPTION

Samples have been collected from sedimentary units within the Hooggenoeg and Mendon formations of the Onverwacht Group of the BGB (Supplemental Fig. 1) and the Strelley Pool Formation of the East Pilbara Terrane (Supplemental Fig. 2). Sample AL03-29B is a silicified tuff (Fig. 1) from the Mendon Formation, and sample H12 is a black banded chert (Fig. 1) from the Hooggenoeg Formation. The third sample, AL04-P10, is a chert (Fig. 1) from the Strelley Pool Formation. Quartz is the predominant phase in all three samples. Hematite, together with some magnetite, is the most common Fe-oxide. Rare carbonates are typically represented by an Fe-rich phase (siderite) that contains minor concentrations of Mg, Mn and Ca, but impure dolomite, rhodochrosite and calcite are also present in samples H12 and AL03-29B. Phosphate minerals are rare in the analyzed samples, and this scarcity is mirrored by a low P_2O_5 content in the whole-rock chemical compositions (Blake et al. 2010; Hofmann et al. 2013). Relatively large and more common (up to 100 μm) apatite crystals were found in cross-cutting chlorite veins in

sample AL03-29B (Fig. 1). These veins are a clear indication of secondary hydrothermal/metamorphic overprinting in this sample. In sample H12, apatite crystals are also associated with a system of chlorite and quartz veins, but the crystals are rather small (< 50 μm) (Fig. 1). In sample AL04-P10, apatite crystals are small (up to 30 μm) and very rare (Fig. 1). Moreover, there is no indication of secondary veining in this sample. The accessory mineral assemblage in all of the samples includes pyrite, as well as both titanite and zircon in the case of sample AL03-29B.

METHODS

Sample preparation was accomplished by using focused ion beam (FIB) milling. Transmission Electron Microscope (TEM) analyses were then conducted to determine the structure of the phosphate minerals and the possible presence of rare earth element (REE)-phosphate inclusions. The FIB-TEM analysis was performed at the German Research Centre for Geosciences (GFZ Potsdam). Areas of 20 × 20 μm on each sample were selected for this study. Firstly, a 1.5-μm protective layer of Pt was deposited to prevent sample damage caused by FIB sputtering and Ga-ion implantation. Then, materials were sputtered out from the frontal and lateral sides of the region of interest, with the FIB operating at an accelerating voltage of 30 kV and a beam current of 30 nA. The frontal surface was then "polished" with a 3-nA FIB, resulting in a final foil thickness of approximately 150 nm. The final size of the TEM foils cut directly from the grains in the thin sections was approximately 20 × 10 × 0.15 μm. The TEM-ready foils were then placed on a perforated carbon film on a copper grid. No carbon coating was required to prevent charging under the electron beam. A detailed description of the sample preparation process has been published by Wirth (2004, 2009). The TEM observations were performed using a FEI Tecnai G2 F20 X-Twin TEM with a Schottky field emitter as an electron source. The TEM was equipped with a Fishione high-angle annular dark field detector (HAADF), an EDAX X-Ray analyzer and a Gatan electron energy-loss spectrometer (EELS). High-resolution lattice fringe images were used to calculate the diffraction pattern (fast Fourier transform, FFT) of the phosphate minerals. The observed d-spacings and angles between adjacent planes were compared with the d-spacings and angles calculated from literature data. The error in the observed d-spacings is within the third decimal place of the measurement. The angles must match within 1° for positive phase identification. The error in the angular measurements from the FFT was < 0.5°.

RESULTS

Four foils were cut from the thin sections representing the three samples for TEM analysis. Two foils (no. #4332 and #4334) were lifted out from the sample of silicified tuff (sample AL03-29B) (Fig. 2a), one foil (no. #4831) was lifted out from the black banded chert (sample H12) (Fig. 2b), and one foil (no. #4803) was lifted out from the other chert (sample AL04-P10) (Fig. 2c).

In all the samples, the apatite crystals are fluorapatite and are composed of slightly misoriented sub-grains. These sub-grains show individual diffraction contrast patterns when tilting the foil in the TEM instrument. The sub-grains are separated by arrays of dislocations that form low-angle grain boundaries (Fig. 2a - 2c). The individual crystals are free of dislocations because the lattice dislocations have migrated to the low-angle grain boundaries by dislocation glide and climb. This process requires annealing at elevated temperatures to activate the diffusion-controlled dislocation climb (Fig. 2a - 2c). In sample AL03-29B, micrometer-sized pores form negative crystals. They are partially filled with solid inclusions up to 200 nm in size (Fig. 2a). The pores are connected via cracks and exhibit triangular dissolution zones (Fig. 2d). In sample H12, the inclusions are elongated, with lengths of up to 300 nm and widths of approximately 15 nm (Fig. 2e). Furthermore, the inclusions show a preferred orientation (Fig. 2e) but are randomly distributed. In samples AL03-29B (Fig. 2a) and AL04-P10 (Fig. 2f), solid inclusions are associated with a system of sub-grains boundaries. Moreover, zones that are rich in nanometer-sized inclusions have been recognized (Fig. 2a, 2b and 2d). Unfortunately, because of the small size of these inclusions, it was not possible to measure their chemical composition. The measured volume always contains a contribution of the chemical composition of the matrix. Additionally, in sample AL03-29B, we observed nano-channel-like structures (Fig. 2d) that were probably created by migrating fluids.

Analysis of the FIB foils from apatites from sample H12 revealed the presence of two (Ca-Y)-phosphate inclusions (Fig. 3a). The first inclusion featured observed angles of 33.6 and 63.0° (Supplemental Tab. S1a), and the second featured observed angles of 65.0 and 53.0°. Structural parameters (d_{hkl}) determined from the diffraction patterns (FFT) (Fig. 3b) indicate that the inclusions could not be indexed as monazite or xenotime but were instead indexed as calcium and yttrium ultraphosphate (Supplemental Tab. S1a), $CaYP_7O_{20}$. This type of ultraphosphate has

previously never been observed in nature. However, the cell parameters of this compound are known from the paper of Hamady and Jouini (1994). $CaYP_7O_{20}$ crystallizes in the monoclinic system. The measured angle between the $(3\bar{1}\bar{1})$ and $(2\bar{1}1)$ planes is 54°, whereas the calculated angle is 54.88°. In addition, the measured angle between the $(3\bar{1}\bar{1})$ and $(10\bar{2})$ planes is of 65°, which corresponds well to the calculated angle of 64.84° (Supplemental Tab. S1a).

In sample AL04-P10, we also observed a (Ca-Y)-phosphate inclusion (Fig. 3c). The diffraction pattern (FFT) (Fig. 3d) of the solid inclusion in this sample yields values of 30°, 31°, 57° and 59° between adjacent lattice planes. The attempt to index the analyzed solid inclusion as monazite or xenotime was not successful. However, it was possible to index the inclusion as calcium and yttrium ultraphosphate, $CaYP_7O_{20}$ (Supplemental Tab. S1b).

Furthermore, in the two FIB foils from sample AL03-29B, we also observed (Ca-Y)-phosphate inclusions (Fig. 3e). The diffraction pattern of the analyzed inclusion in sample AL03-29B yielded values of 39.9 and 49.8° (Supplemental Tab. S2). Attempts to index the observed phase as monazite, xenotime or monoclinic $CaYP_7O_{20}$ were not successful (Supplemental Tab. S2). The solid inclusion observed in this sample was identified as $Ca_3Y(PO_4)_3$. Unfortunately, because of the size of the inclusion, we were able to obtain only one diffraction pattern that did not overlap with the host apatite.

The absence of an amorphous layer at the phase boundary between the host apatite and the inclusions is a characteristic feature of the interfaces observed in high-resolution images of samples AL03-29B and H12 (Fig. 3a and 3e).

Since apatite is composed mostly of calcium phosphate, special care was taken to rule out interference from the host. Therefore, only the largest inclusions were used for energy dispersive X-ray (EDX) analyses. Analyses of the observed solid inclusions in all of the samples indicate that they are composed of calcium and yttrium phosphate (Fig. 3g - 3i). Although differences in the REE composition of the (Ca-Y)-phosphate phases may exist, it was not possible to measure such differences with EDX measurements.

DISCUSSION

In the apatite structure, (REE+Y) substitutions are charge balanced through coupled substitutions: $Si^{4+} + (REE+Y)^{3+} = P^{5+} + Ca^{2+}$ and $Na^{+} + (REE+Y)^{3+} = 2Ca^{2+}$ (Pan and Fleet 2002). During the alteration of apatite, various fluids can cause the preferential removal of Na

and/or Si from the apatite-fluid system without the removal of REEs. Removal of only Na and/or Si results in a charge imbalance. The available (REE+Y) concentration then increases. Once super-saturated conditions form, the REEs can react with phosphate and cause possible nucleation and growth of (REE+Y)-phosphate phases, such as monazite and xenotime. This process occurs via the two following mass transfer reactions: $[Ca_{5-2x}, Na_x, REE_x]P_3O_{12}F + x\ [2\ Ca^{2+} + P^{5+}]$ (from the fluid) = $Ca_5P_3O_{12}F + x\ REEPO_4 + x\ [Na^+]$ (into the fluid) and $[Ca_{5-y}, REE_y][P_{3-y}, Si_y]O_{12}F + y\ [Ca^{2+} + 2\ P^{5+}]$ (from the fluid) = $Ca_5P_3O_{12}F + y\ REEPO_4 + y\ [Si_{4+}]$ (into the fluid) (Harlov 2015). The final composition of the (REE+Y)-phosphate inclusions is dependent on additional parameters, such as the chemistry of the altering fluid (which can mobilize some of the elements) and the P-T conditions of the alteration (Harlov and Föster 2003). Furthermore, inclusions can be created by exsolution processes (Sun et al. 2007). Inclusions can also precipitate first and can later be overgrown by the crystallizing host phase (Kohn at al. 2005).

According to experiments (e.g., Szuszkiewicz and Znamierowska 1990; Fukuda et al. 2006; Matraszek and Radomińska 2014), the existence of cubic $Ca_3Y(PO4)_3$ is limited to temperatures exceeding 1215 °C. In contrast, the monoclinic $(Ca_{0.726}Y_{0.274})(Ca_{0.274}Y_{0.726})P_7O_{20}$ phase can form at approximately 450 °C (Hamady and Jouini 1994). However, there are no experimental data describing the influence of additional parameters, such as pressure, on the stability of these phases.

In samples AL03-29B and H12, apatite crystals are associated with systems of cross-cutting veins filled with chlorite group minerals. Blake et al. (2010) have reported a $\delta^{18}O$ value of 9.3‰ for apatite crystals from the same location as sample AL03-29B. This relatively low $\delta^{18}O$ value, together with evidence for secondary veining, indicates that these phosphates formed from hydrothermal or metamorphic fluids. Moreover, the $\delta^{18}O$ value of 9.3‰ was the lowest of all the samples analyzed from the BGB. Thus, this value may be representative of phosphate derived from a secondary fluid.

Different TEM imaging modes (bright field – BF, dark field – DF, and lattice fringe imaging) provided information regarding the formation and transformation pathways of apatite crystals. Notably, all of the samples are characterized by visible metamorphic alterations (Fig. 2a - 2c). The apatite crystals are composed of sub-grains separated by dislocation arrays that form low-angle grain boundaries (Fig. 2a - 2c). The altered apatite exhibits a porous texture (Fig. 2a -

2d) related to partial dissolution, which most likely developed by intrusive fluids penetrating the apatite structure. The (Ca-Y)-phosphate inclusions in sample H12 show a preferred orientation (Fig. 2e). Previous researchers (Pan et al. 1993; Pan and Fleet 2002; Harlov 2015) have noted that REE-phosphate inclusions, e.g., monazite, can be highly elongated. This elongation often occurs along the *b* axis and parallel to the *c* axis of the host apatite, suggesting an epitaxial relationship (Harlov 2015). An orientation relationship was not visible in the case of $CaYP_7O_{20}$ phase but was observed in sample AL03-29B. The $(\bar{2}\bar{1}1)$ and (022) vectors of $Ca_3Y(PO4)_3$ are parallel to the $(10\bar{1}0)$ and (0001) vectors, respectively, of the apatite (Fig. 2f). Furthermore, the *d*-spacings of 4.0144 Å for $(\bar{2}\bar{1}1)$ and 3.4766 Å for (022) are approximately half of those of 7.8 Å for $(10\bar{1}0)$ and 6.67 Å for (0001) in apatite, respectively (Supplemental Tab. S2). According to Harlov et al. (2007), this phenomenon can be explained by a topotactic reaction, i.e., a chemical solid-state reaction in which the orientations of the product crystals are determined by the orientation of the initial crystal. In this case, the formation of $Ca_3Y(PO4)_3$ does not involve exsolution from a solid solution; instead, the formation of $Ca_3Y(PO4)_3$ involves fluid-aided growth of a separate phase that utilizes the available chemical components. This growth can be referred to as topotactic because the formation and growth of one phase (i.e., cubic $Ca_3Y(PO4)_3$) within a second phase (i.e., apatite) can be required to accommodate the differences in the lattice parameters and *d*-spacings. In other cases, the $Ca_3Y(PO4)_3$ grains may grow with random orientations as long as they have little or no contact with the surrounding host apatite. Whether topotactic growth of $Ca_3Y(PO4)_3$ occurs in the host apatite appears to be a direct function of the reactivity of the fluid causing the dissolution-reprecipitation process in apatite. Furthermore, topotactic growth might also explain the lack of an amorphous rim at the phase boundary interface between the $Ca_3Y(PO4)_3$ and $CaYP_7O_{20}$ inclusions and the surrounding apatite (Fig. 2a and 2e).

Traces of secondary alteration, e.g., solid inclusions associated with the system of sub-grain boundaries and the presence of porosity, suggest that the $CaYP_7O_{20}$ inclusions originated via dissolution-reprecipitation processes.

The rare presence of cubic $Ca_3Y(PO_4)_3$ can be explained by its high-formation temperature. Data on the synthesis and the stability of synthetic $Ca_3Y(PO_4)_3$ suggest that crystallization of this phase begins at temperatures above 1215 °C at atmospheric pressure (Szuszkiewicz and Znamierowska 1990; Fukuda et al. 2006; Matraszek and Radomińska 2014).

Below this temperature, a decomposition reaction ($Ca_3Y(PO_4)_3 \rightarrow \beta\text{-}Ca_3(PO_4)_2 + YPO_4$) occurs. However, rapid cooling to temperatures below 250 °C may preserve the $Ca_3Y(PO_4)_3$ phase at ambient temperatures. Although the $Ca_3Y(PO_4)_3$ phase was observed in tuff, this sample is unlikely to have experienced a temperature of 1215 °C. Additionally, sample AL03-29B is characterized by visible metamorphic alterations (Fig. 2a and 2d). For example, the apatite crystals are composed of sub-grains separated by arrays of dislocations (Fig. 2a), and the presence of channel-like structures (Fig. 2d) used by migrating fluids is indicative of dissolution-reprecipitation processes. The pores and nano-channel-like structures played important roles as sites of nucleation and growth of (Ca-Y)-phosphate inclusions.

IMPLICATIONS

Accessory minerals are essential REE carriers in many environments. Their internal zoning, compositional variations and alterations can provide valuable information on the environmental conditions during the formation of both terrestrial and extraterrestrial rocks. Among phosphate and silicate minerals rich in REEs and Y, apatite is the most widespread accessory phase in most rocks. Although apatite commonly precipitates as a primary accessory phase in sedimentary rocks and, more commonly, crystallizes in magmatic and metamorphic environments, subsequent reactions with fluids can cause dissolution and the formation of secondary mineral assemblages (Harlov 2015; Webster and Poccoli 2015). The most common products of this alteration are monazite and/or xenotime (Harlov and Förster 2003; Harlov et al. 2005). Therefore, apatite compositions can be used to evaluate the formation environment and subsequent evolution of abiotic Archean environments. The existence of (Ca-Y)-phosphate inclusions indicate that the rocks of the BGB and Pilbara Craton, at least partially, experienced secondary alteration. This finding is consistent with the oxygen isotope data (Blake et al. 2010) suggesting that the BGB contains early and late generations of phosphates. The late-generation apatite precipitated under the influence of secondary fluids and hydrothermal veining, whereas the early-generation apatite was not associated with any veining. The (Ca-Y)-phosphate inclusions were observed only in samples that experienced hydrothermal alteration and in apatite crystals that were associated with veining. Therefore, samples in which apatite crystals are randomly distributed might be more suitable for estimating the environmental conditions of abiotic Archean environments. The (Ca-Y)-phosphate inclusions in the sample from the Strelley

Pool Chert Formation of the Pilbara Craton occur in apatite crystals in sedimentary rocks. In the case of this sample, no association with secondary veins was observed. Therefore, the question of whether these apatite crystals experienced secondary alteration or preserve their primordial signature might be crucial for future research on phosphates from the Pilbara Craton.

This study also provides information on the composition of the altering fluids. In the experiments conducted by Harlov and Förster (2003), REE-phosphate phases were observed as inclusions in experimentally altered fluorapatite only in the presence of H_2O and KCl brines at temperatures below 900 °C. Nevertheless, the authors found that the H_2O component, not the K^+ or Cl^- components, in the solution was responsible for the generation of the REE-phosphate inclusions. Furthermore, experimental work (Migdisov et al. 2009; Migdisov and Williams-Jones 2014) has shown that hydrothermal fluids preferentially mobilize light REEs (LREEs) and Y over heavy REEs (HREEs) in the form of REE-chloride and REE-fluoride complexes. Since the experiments by Harlov and Förster (2003) indicate that REE-phosphates did not nucleate in Cl-rich environments, the REE-F complexes in an H_2O solution and the specific budget of REEs and Y in the apatite were likely responsible for the nucleation and formation of the (Ca-Y)-phosphate phases in the Archean rocks of the BGB and Pilbara Craton.

Finally, our research identified two (Ca-Y)-phosphate phases never previously described in nature. The first was observed as solid inclusions in apatite crystals from samples of metachert and black banded chert. This phase is monoclinic, has a formula of $CaYP_7O_{22}$, and crystallizes at approximately 450 °C. The second new phase, cubic $Ca_3Y(PO_4)_3$, was observed in apatite crystals from a sample of silicified tuff from the Mendon Formation in the BGB. Its existence has been previously reported by Szuszkiewicz and Znamierowska (1990), Fukuda et al. (2006) and Matraszek and Radomińska (2014). According to previous research, the crystallization of this phase begins at temperatures above 1215 °C at atmospheric pressure. However, this study shows that temperature is not the only parameter controlling the crystallization of this phase. The most likely scenario is that both (Ca-Y)-phosphate phases originate from dissolution-reprecipitation processes.

ACKNOWLEDGEMENTS

We are deeply grateful to R. Tartèse and E. Nakamura for their helpful and inspiring reviews, which helped us to significantly improve our manuscript. We very much appreciate the efficient

and helpful editorial comments of I. Swainson. The research was funded by the Polish NCN grant no. 2013/11/B/ST10/04753 and was supported by COST Action TD1308 "ORIGINS".

REFERENCES CITED

Furnes, H., De Wit, M.J., Robins, B., and Sandsta, N.R., (2011) Volcanic evolution of the upper Onverwacht Suite, Barberton greenstone belt, South Africa. Precambrian Research, 186, 28–50.

Harlov, D.E., and Förster, H-J. (2003) Fluid-induced nucleation of (Y+REE)-phosphat minerals within apatite: nature and experiment. Part II. Fluorapatite. American Mineralogist, 88, 1209-1229

Harlov, D.E., Marschall, H.R., and Hanel, M. (2007) Fluorapatite-monazite relation-ships in granulite-facies metapelites, Schwarzwald, southwest Germany. Mineralogical Magazine, 71, 223-234

Harlov, D.E., Wirth, R., and Förster, H.J. (2005) An experimental study of dissolution-reprecipitation in fluorapatite: Fluid infiltration and the formation of monazite. Contributions to Mineralogy and Petrology, 150, 268–286.

Hickman, A.H. (2008) Regional review of the 3426–3350 Ma Strelley Pool Formation, Pilbara Craton, Western Australia. Western Australia Geological Survey Record, 2008/15, 50

Hughes, J.M., and Rakovan, J. (2002) The crystal structure of apatite, $Ca_5(PO_4)_3(F,OH,Cl)$. In M.J. Kohn, J. Rakovan and J.M. Hughes, Eds., Phosphates—Geochemical, geobiological, and materials importance, 48, p. 13–49. Reviews in Mineralogy and Geochemistry, Mineralogical Society of America, Chantilly, Virginia.

Hofmann, A., Bolhar, R., Orberger, B., and Foucher, F. (2013) Cherts of the Barberton Greenstone Belt, South Africa: Petrology and trace-tlement geochemistry of 3.5 to 3.3 Ga old silicified volcaniclastic sediments. South African Journal of Geology, 116, 297–322.

Kröner, A., Byerly, G.R. and Lowe, D.R. (1991) Chronology of early Archaean granite-greenstone evolution in the Barberton Mountain Land, South Africa, based on precise dating by single zircon evaporation. Earth Planetary Science Letters, 103, 41–54.

Kamo, S.L., and Davis, D.W. (1994) Reassessment of Archean crustal development in the Barberton Mountain Land, South Africa, based on U–Pb dating. Tectonics, 13, 167–192

Knauth, L.P., and Lowe, D.R. (2003) High Archean climatic temperature inferred from oxygen isotope geochemistry of cherts in the 3.5 Ga Swaziland Supergroup, South Africa. Geological Society of America Bulletin, 115, 566–580.

Kohn, M.J., Wieland, M.S., Parkinson, C.D., and Upreti, B.N. (2005) Five generations of monazite in Langtang gneisses: implications for chronology of the Himalayan metamorphic core. Journal of Metamorphic Geology, 23, 399-406

Matraszek, A., and Radomińska, E.J. (2014) The revised phase diagram of the $Ca_3(PO_4)_2$–YPO_4 system. The temperature and concentration range of solid-solution phase fields. Journal of Thermal Analysis and Calorimetry, 117, 101 – 108

Mbarek, A., Graia, M., Chadeyron, G., Zambon, D., Bouaziz, D., and Fourati, M. (2009) Synthesis and crystal structure determination of yttrium ultraphosphate YP5O14. Journal of Solid State Chemistry, 182, 509–516.

Migdisov, A.A., and Williams-Jones, A.E. (2014) Hydrothermal transport and deposition of the rare earth elements by fluorine-bearing aqueous liquids. Mineralium Deposita, 49, 987–997.

Migdisov, A.A., Williams-Jones, A.E., and Wagner, T. (2009) An experimental study of the solubility and speciation of the Rare Earth Elements (III) in fluoride- and chloride-bearing aqueous solutions at temperatures up to 300 °C. Geochimica et Cosmochimica Acta, 73, 7087–7109.

Ni, Y., Hughes, J.M., and Mariano, A.N. (1995) Crystal chemistry of the monazite and xenotime structures. American Mineralogist, 80, 21-26.

Pan, Y., and Fleet, M.E. (2002) Compositions of the apatite-group minerals: Substitution mechanisms and controlling factors. Reviews in Mineralogy and Geochemistry, 48, 13-49

Pan, Y., Fleet, M.E., and Macrae, N.D. (1993) Oriented monazite inclusions in apatite porphyroblasts from the Hemlo gold deposit, Ontario, Canada. Mineralogical Magazine, 57, 697-707

Sun, X., Tang, Q., Sun, W., Xu, L., Zhai, W., Liang, J., Liang, Y., Shen, K., Zhang, Z., Zhou, B., and Wang, F. (2007) Monazite, iron oxide and barite exsolution in apatite aggregates from CCSD drillhole eclogite and their geological implications. Geochemica et Cosmochimica Acta, 71 (11), 2896-2905

Szuszkiewicz, W., and Znamierowska, T. (1990) The system YPO_4-$Ca_3(PO_4)_2$. Journal of Solid State Chemistry, 88 (2), 406-410

Tice, M.M., Bostick, B.C. and Lowe, D.R. (2004) Thermal history of the 3.5–3.2 Ga Onverwacht and Fig Tree Groups, Barberton greenstone belt, South Africa, inferred by Raman microspectroscopy of carbonaceous material. Geology 32, 37–40.

van Kranendonk, M.J., Philippot, P., Lepot, K., Bodorkos, S., and Pirajno, F. (2008): Geological setting of Earth's oldest fossils in the c. 3.5 Ga Dresser Formation, Pilbara Craton, Western Australia. Precambrian Research, 167, 93-124. doi. 10.1016/j.precamres.2008.07.003.

Wacey, D. (2010) Stromatolites in the ≈3400 Ma Strelley Pool Formation, Western Australia: examining biogenicity from the macro- to the nano-scale. Astrobiology, 10, 381–395.

Webster, J.D., and Piccoli, P.M. (2015) Magmatic Apatite: A Powerful, Yet Deceptive, Mineral. Elements, 11, 177–182.

Wirth, R. (2004) A novel technology for advanced application of micro- and nanoanalysis in geosciences and applied mineralogy. European Journal of Mineralogy, 16, 863–876

—— (2009) Focused ion beam (FIB) combined with SEM and TEM: Advanced analytical tools for studies of chemical composition, microstructure and crystal structure in geomaterials on a nanometre scale. Chemical Geology, 261, 217–229

Figure list:

Figure 1. Back-scatter electron images of phosphate phases in Barberton samples. Black, dashed line in the picture of sample H12 indicates quartz vein. No indication of secondary veining has been observed in sample AL04-P10.

Figure 2. Post-magmatic alterations and (Ca-Y)-phosphate inclusions in apatite crystals. a) HAADF image of a (Ca-Y)-phosphate inclusion in apatite in sample AL03-29B. Black dashed lines show low-angle grain boundaries. Furthermore, "fingerprints" of metasomatic alterations, such as pores partially filled by solid inclusions (black arrow) and fluid inclusion-rich zones (white dashed circles), are visible. b) Bright-field image of apatite sub-grains separated by dislocation arrays (white arrow) and by parallel (left black arrow) and simply curved (right black arrow) low-angle grain boundaries (sample H12). c) Bright-field image of altered apatite in sample AL04-P10. Black arrows indicate porosity, whereas

dashed lines depict sub-grain boundaries. The dashed rectangle shows the position of Figure 1f. Qtz stands for quartz. d) HAADF image of altered apatite in sample AL03-29B. Connected cracks, triangular dissolution zones (black arrows), fluid inclusion-rich zones (white, dashed circles) and nano-channel-like structures (black, dashed lines) are visible. e) Bright-field image of monoclinic (Ca-Y)-phosphate inclusions in sample H12. Note the direction of the orientation and elongation of the inclusions (black arrow). f) HAADF image of (Ca-Y)-phosphate inclusions (white arrows) in apatite in sample AL04-P10.

Figure 3. a) Lattice fringe image of the elongated, monoclinic (Ca-Y)-phosphate inclusion in host apatite (sample H12). Note the lack of an amorphous rim (black arrow) at the phase boundary interface between the (Ca-Y)-phosphate inclusions and the surrounding apatite (sample H12). b) Indexed diffraction pattern (FFT) taken from the area in (a). c) Lattice fringe image of monoclinic (Ca-Y)-phosphate inclusion in host apatite (sample AL04-P10). The parallel dark contrasts are Moiré contrast due to an overlap of the Ca-Y phosphate lattice fringes with those of the host. d) Indexed diffraction pattern (FFT) taken from the area in (c). e) Lattice fringe image of the phase boundary between apatite and cubic (Ca-Y)-phosphate. Note the lack of an amorphous rim (black arrow) at the phase boundary interface between the (Ca-Y)-phosphate inclusions and the surrounding apatite (sample AL03-29B). f) Indexed diffraction pattern (FFT) taken from the area in (e). g) EDX analysis of monoclinic (Ca-Y)-phosphate phase in sample H12. h) EDX analysis of monoclinic (Ca-Y)-phosphate phase in sample AL04-P10. i) EDX analysis of cubic (Ca-Y)-phosphate phase in sample AL03-29B.

Figure 1.

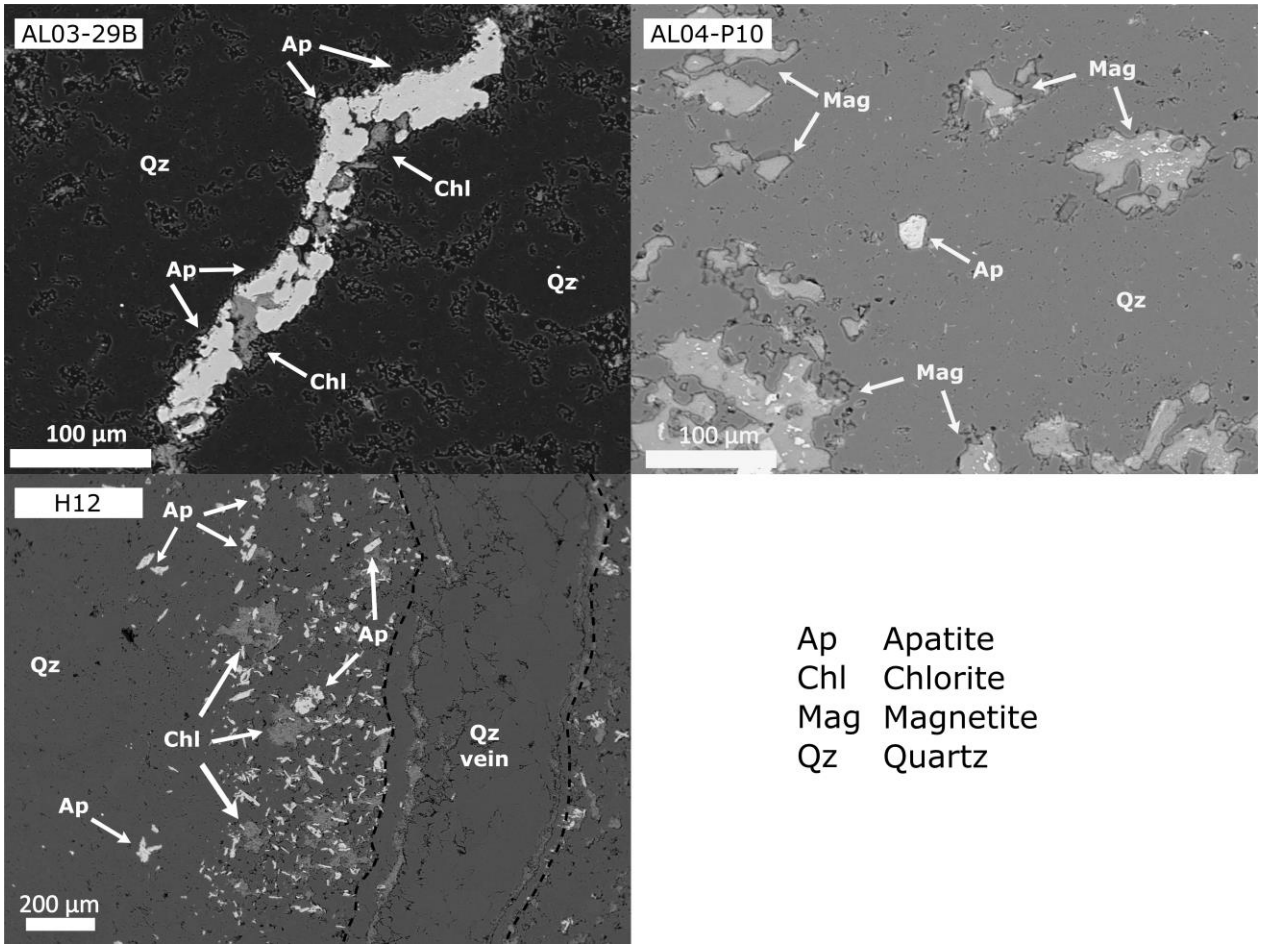

Figure 2.

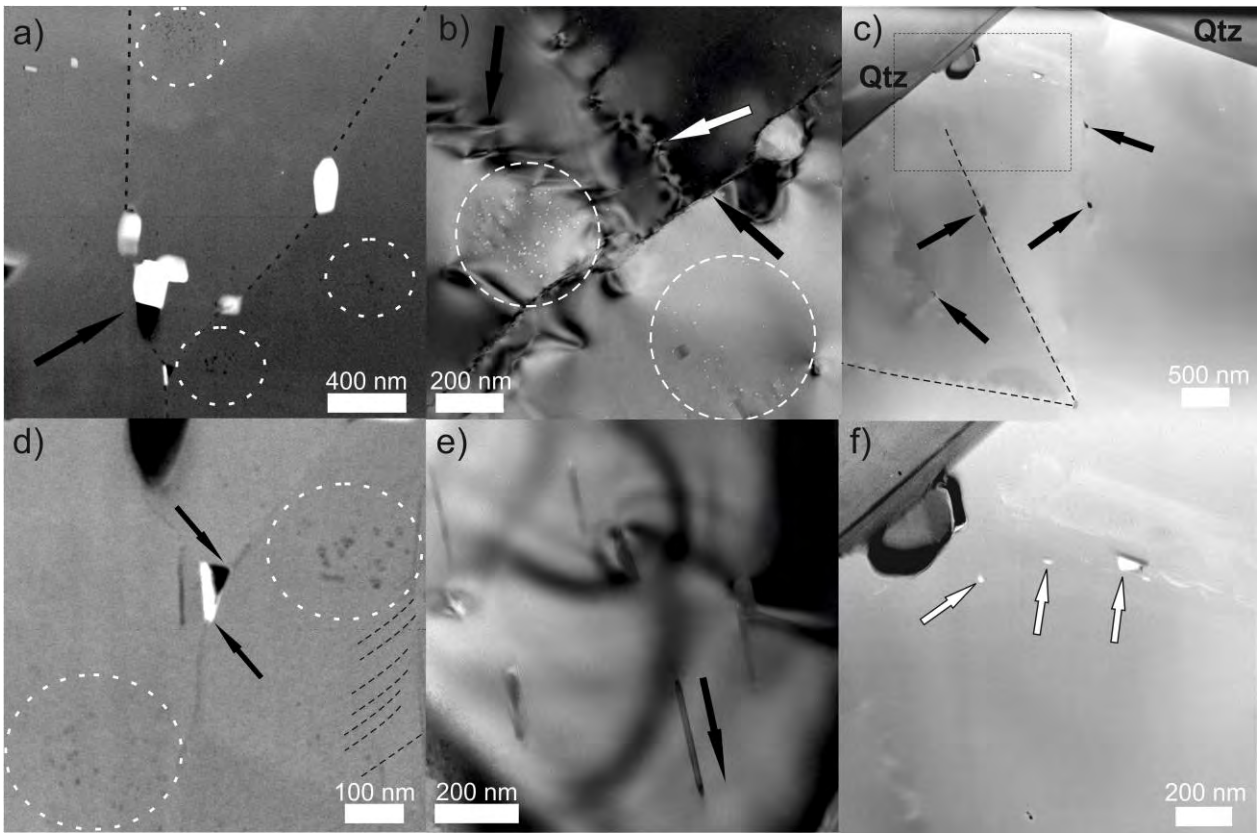

Figure 3.